AGU PUBLICATIONS

JGR

Journal of Geophysical Research: Planets

RESEARCH ARTICLE
10.1002/2015JE004948

Key Points:
- Model the Phobos neutral and ionized torus produced by sputtering, micrometeoroid bombardment, and PSD
- Most ejected species form torus concentric with Phobos orbit; aluminum forms a small corona
- Both neutral densities and pickup ion fluxes are very low; no perturbation to ambient environment

Correspondence to:
A. R. Poppe,
poppe@ssl.berkeley.edu

Citation:
Poppe, A. R., S. M. Curry, and S. Fatemi (2016), The Phobos neutral and ionized torus, *J. Geophys. Res. Planets*, *121*, doi:10.1002/2015JE004948.

Received 24 SEP 2015
Accepted 19 APR 2016
Accepted article online 25 APR 2016

The Phobos neutral and ionized torus

A. R. Poppe[1,2], S. M. Curry[1], and S. Fatemi[1,2]

[1]Space Sciences Laboratory, University of California, Berkeley, California, USA, [2]Solar System Exploration Research Virtual Institute, NASA Ames Research Center, Moffett Field, California, USA

Abstract Charged particle sputtering, micrometeoroid impact vaporization, and photon-stimulated desorption are fundamental processes operating at airless surfaces throughout the solar system. At larger bodies, such as Earth's Moon and several of the outer planet moons, these processes generate tenuous surface-bound exospheres that have been observed by a variety of methods. Phobos and Deimos, in contrast, are too gravitationally weak to keep ejected neutrals bound and, thus, are suspected to generate neutral tori in orbit around Mars. While these tori have not yet been detected, the distribution and density of both the neutral and ionized components are of fundamental interest. We combine a neutral Monte Carlo model and a hybrid plasma model to investigate both the neutral and ionized components of the Phobos torus. We show that the spatial distribution of the neutral torus is highly dependent on each individual species (due to ionization rates that span nearly 4 orders of magnitude) and on the location of Phobos with respect to Mars. Additionally, we present the flux distribution of torus pickup ions throughout the Martian system and estimate typical pickup ion fluxes. We find that the predicted pickup ion fluxes are too low to perturb the ambient plasma, consistent with previous null detections by spacecraft around Mars.

1. Introduction

Neutral particle emission from airless surfaces is a fundamental process that occurs throughout the solar system. Several processes contribute to the ejection of neutrals, including charged particle sputtering [e.g., *Biersack and Eckstein*, 1984; *Wurz et al.*, 2007], micrometeoroid impact vaporization (MIV) [*Eichhorn*, 1976], photon-stimulated desorption [*Yakshinskiy and Madey*, 1999, 2004], and thermal sublimation/desorption. Reflection of incident charged particles as energetic neutral atoms is also known to occur [e.g., *Wieser et al.*, 2009; *Rodríguez et al.*, 2012]. At large bodies, such as Earth's Moon or the larger moons of the outer planets, many neutral species are ejected with velocities below escape speed and thus remain bound, forming so-called surface-bounded exospheres. To date, such neutral exospheres have been detected via a variety of methods at Mercury [e.g., *Potter and Morgan*, 1985, 1986; *McClintock et al.*, 2008], the Moon [*Hoffman et al.*, 1973; *Feldman et al.*, 2012; *Stern et al.*, 2012; *Benna et al.*, 2015], the Galilean satellites [e.g., *Hall et al.*, 1995; *Carlson*, 1999; *Feldman et al.*, 2000; *Cunningham et al.*, 2015], and some of the Saturnian satellites [*Teolis et al.*, 2010; *Tokar et al.*, 2012]. Neutral coronae around bodies too gravitationally weak to keep ejected neutrals bound have also been theorized yet not detected to date; these objects include asteroids [e.g., *Morgan and Killen*, 1998; *Schläppi et al.*, 2008; *Altwegg et al.*, 2012] and Mars' moons Phobos and Deimos [*Soter*, 1971; *Mura et al.*, 2002; *Cipriani et al.*, 2011]. Since the surfaces of each of these bodies are directly exposed to the ambient space environment, detection and characterization of these exospheres or coronae may deliver detailed knowledge about both the surface composition and the nature of the fundamental processes that govern surface interactions.

Mars possesses two small moons, Phobos and Deimos, believed to be either captured asteroids from the main asteroid belt (or beyond) [e.g., *Hartmann*, 1987; *Pollack et al.*, 1979; *Pajola et al.*, 2013] or accretionary products from either Mars' primordial formation [*Veverka and Burns*, 1980, and references therein] or from a late-era impact [*Craddock*, 2011; *Rosenblatt and Charnoz*, 2012; *Witasse et al.*, 2014; *Citron et al.*, 2015]. Neither Phobos nor Deimos contain sufficient mass to keep ejected neutrals gravitationally bound; thus, we do not expect, and no observational evidence has otherwise suggested, that Phobos and Deimos possess surface-bounded exospheres. Despite this, it has been long suspected that neutrals ejected from Phobos and Deimos, while not bound to the moons themselves, may still be bound inside Mars' gravitational well and, thus, would form a tenuous, extended set of tori around Mars [*Soter*, 1971]. Early observations by the Phobos-2 mission suggested the presence of such tori indirectly via the detection of anomalous perturbations to the magnetic field

and plasma environment of Mars roughly correlated with the positions of Phobos and Deimos [*Dubinin et al.*, 1991]; however, later observations by the Mars Global Surveyor (MGS) mission failed to detect any statistically significant correlation between observed plasma/field anomalies and the orbits or locations of the moons [*Øieroset et al.*, 2010], casting doubt on the interpretation of Phobos-2 observations as evidence of Phobos and/or Deimos tori. Additionally, while the Mars Express (MEX) spacecraft has observed solar wind proton reflection from Phobos' surface [*Futaana et al.*, 2010], no detection of Phobos-originating neutrals or pickup ions has been reported to date by the MEX mission [*Witasse et al.*, 2014].

Production of the putative Phobos and Deimos tori has been postulated by a number of different processes, including direct water outgassing [*Fanale and Salvail*, 1989], absorption and reemission of Martian coronal atomic oxygen [*Ip and Banaszkiewicz*, 1990], micrometeoroid impact vaporization, and charged particle sputtering from both the solar wind [*Cipriani et al.*, 2011] and heavy Martian pickup ions (mainly O^+) [*Poppe and Curry*, 2014]. For example, *Mura et al.* [2002] assumed a water outgassing source as postulated by *Fanale and Salvail* [1989] with a production rate of $Q = 10^{23}$ s^{-1} and characteristic neutral temperature of $T = 250$ K. Their predicted torus structure resembled a thin ring of neutrals only 200 km in radius colocated along the Phobos orbit at 2.7 R_M (≈9150 km) with peak densities of nearly 10^5 cm^{-3}. The relatively high production rate assumed from direct outgassing of water vapor has been ruled out by later observations [*Øieroset et al.*, 2010], and more recent estimates for the production rate due to charged particle sputtering are on the order of 10^{19} s^{-1} [*Cipriani et al.*, 2011; *Poppe and Curry*, 2014]. Using this lower production rate, *Cipriani et al.* [2011] modeled the density of several neutral species representative of Phobos' surface (O, Na, Mg, Al, Si, and Fe) [*Vernazza et al.*, 2010] and found densities between 10^{-4} and 10^{-1} cm^{-3} within 500 km of Phobos. Such small neutral densities are far too low to be detected with in situ neutral mass spectrometers, yet it was estimated that remote observations of solar scattering lines could yield a positive detection in the case of Mg [*Cipriani et al.*, 2011]. To date, however, the possible detection of the Phobos torus via pickup ions has only recently been discussed [*Poppe and Curry*, 2014], motivated by the arrival at Mars of the Mars Atmosphere and Volatile EvolutioN (MAVEN) mission [*Jakosky et al.*, 2014]. Detection of torus pickup ions is an attractive method of confirming the presence of the torus as charged particle detectors are typically capable of much lower count sensitivity than neutral mass spectrometers.

Thus, in order to further define the neutral and ionized components of the Phobos torus, we have performed detailed simulations using a combination of a neutral Monte Carlo dynamics model and a hybrid plasma/ionized test particle model. These models allow us to make quantitative estimates of the spatial distribution and absolute magnitude for both the density of torus neutrals and the flux of torus pickup ions. In section 2, we describe the details and assumptions for both models and present the results for the neutral and ionized components in sections 2 and 3, respectively. Finally, we discuss the results and conclude in section 4.

2. Phobos Neutral Torus

2.1. Neutral Monte Carlo Model

In order to investigate the three-dimensional structure of the Phobos neutral torus, we have developed a Monte Carlo model that traces the trajectories of individual neutral atoms after their ejection from the surface of Phobos due to either charged particle sputtering, micrometeorite impact vaporization (MIV), or photon-stimulated desorption (PSD) in the case of Na only [*Yakshinskiy and Madey*, 1999, 2004]. Table 1 lists the various characteristics of the modeled neutral species relevant for both the neutral Monte Carlo and test particle models (see section 3.2). The surface composition of Phobos can be approximated by that of a D-type asteroid, neglecting the Stickney region of Phobos which appears compositionally different [*Rivkin et al.*, 2002; *Vernazza et al.*, 2010]. The assumed composition for Phobos is dominantly silicate in nature with an additional strong iron presence, as well as several more minor species. In sum, we model six species: O, Na, Mg, Al, Si, and Fe. We note that while oxygen is the dominant component of our assumed Phobos surface material by number, any oxygen torus from Phobos will most likely be overwhelmed by the presence of Martian coronal oxygen, especially during solar maximum conditions [e.g., *Chaufray et al.*, 2007]. Nevertheless, the other five species are not expected to have origins from Mars itself and, thus, provide a set of unique "tracer" species that, if detected, are highly suggestive of origins from Phobos.

The main force acting on the neutral atoms is gravity from Mars, as the very small gravitational perturbations from Phobos and Deimos can be safely neglected. Solar radiation pressure is also included for Na.

Table 1. The Mass, Mass Fraction, Number Fraction, Production Rates, Ionization Rates, Peak Neutral Density, and Peak Pickup Ion Flux for the Dominant Atomic Species Generated Through Sputtering at Phobos

	O	Na	Mg	Al	Si	Fe
Mass (amu)	16	23	24.3	27	28	56
Mass fraction[a,b]	0.41	0.005	0.10	0.017	0.13	0.21
Number fraction	0.64	0.005	0.14	0.015	0.11	0.09
Neutral production rates (s^{-1})						
Sputtered production rate	1.2×10^{19}	1.0×10^{17}	2.9×10^{18}	3.1×10^{17}	2.2×10^{18}	1.8×10^{18}
PSD production rate	–	2.7×10^{18}	–	–	–	–
Ionization rates (s^{-1})						
Photo-ionization rate[c]	2.0×10^{-7}	3.4×10^{-6}	4.0×10^{-7}	5.6×10^{-4}	1.6×10^{-5}	6.1×10^{-6}
EI ionization rate[d]						
Solar wind	1.9×10^{-8}	2.3×10^{-7}	2.2×10^{-7}	3.4×10^{-7}	2.3×10^{-7}	2.1×10^{-7}
Magnetosheath	1.5×10^{-6}	3.3×10^{-6}	4.0×10^{-6}	7.3×10^{-6}	7.3×10^{-6}	4.4×10^{-6}
Magnetotail	1.0×10^{-8}	5.1×10^{-8}	5.7×10^{-8}	9.5×10^{-8}	7.9×10^{-8}	5.7×10^{-8}
CX ionization rate[e]	9.6×10^{-8}	3.6×10^{-7}	1.2×10^{-7}	1.2×10^{-7}	1.2×10^{-7}	1.2×10^{-7}
Peak neutral density (cm^{-3})	1.6×10^{-3}	3.8×10^{-4}	5×10^{-4}	4.3×10^{-5}	3.5×10^{-4}	4.4×10^{-4}
Peak pickup ion flux ($cm^{-2}\ s^{-1}$)[f]	125	15	31	6	10	14

[a] *Vernazza et al.* [2010].
[b] *Cipriani et al.* [2011].
[c] Assuming solar median conditions at 1.5 AU [*Huebner and Mukherjee*, 2015].
[d] See text for electron temperature and density.
[e] Assuming $n_{sw} = 3\ cm^{-3}$, $v_{sw} = 400$ km/s.
[f] Assuming median solar wind/UV conditions.

Based on calculations of the radiation pressure acceleration of Na at Earth's Moon [*Smyth and Marconi*, 1995], we extrapolate to 1.5 AU and adopt an acceleration of $a = 2.0\ cm\ s^{-2}$ in the antisunward direction for Na atoms at Mars/Phobos. We omit the axial tilt of Mars with respect to the ecliptic plane (≈25°). Neutral particles for each species are launched from the surface of Phobos with a velocity distribution dependent on the relevant process: for charged particle sputtering a Sigmund-Thompson distribution is used [*Thompson et al.*, 1968; *Sigmund*, 1969]; for MIV, a Maxwellian velocity distribution with temperature $T = 3000$ K is used [*Eichhorn*, 1976]; and for photon-stimulated desorption, a Maxwellian with temperature $T = 2000$ K is used [*Yakshinskiy and Madey*, 2004]. MIV-produced neutrals are released isotropically from the surface, while both sputtered neutrals and PSD-generated Na are released from the dayside of Phobos with a cosine solar zenith angle distribution. All particles are assigned an initial weight, w_i, based on their ejection velocity relative to the chosen velocity distribution, i.e., $w_i = f(v_e)$, where $f(v)$ is the chosen velocity distribution (MIV, sputtering, or PSD) and v_e is the ejection velocity of the neutral from the surface of Phobos. As time evolves the weight for each individual neutral is decreased according to the total ionization rate of each species as $w_{i+1} = w_i e^{-dt/\tau}$, where dt is the Monte Carlo time step and τ is the total ionization lifetime for a specific species (see discussion of ionization lifetimes in section 2.2 below). Neutral particles are traced until one of three conditions occurs: (1) the particle hits Mars, (2) the particle leaves the simulation domain (i.e., is lost from the Martian system), or (3) the weight of the particle falls below 10^{-6} of its original weight due to ionization. Throughout the simulation of each individual particle, we also track the instantaneous location of Phobos around Mars. At times when Phobos passes four locations along its orbit (noon, dusk, midnight, and dawn), the density and flux of the neutral particles are recorded in three-dimensional arrays with size $20 \times 20 \times 20\ R_M$ centered on Mars with cell size $0.1 R_M$. Each simulation includes 5×10^7 particles, sufficient enough to fully populate the velocity distribution.

2.2. Neutral Ionization Rates

In order to determine the ionization loss rates from the neutral torus, we include photo-ionization, electron impact ionization, and solar wind proton charge exchange ionization for all six neutral species. Photo-ionization rates at 1.5 AU are calculated from *Huebner and Mukherjee* [2015]; solar median values for each species are listed in Table 1. Electron impact (EI) ionization cross sections are taken from *Bartlett and Stelbovics* [2002, 2004] for all six species. Figure 1a shows the electron impact ionization cross sections as a function of electron impact energy. EI ionization of oxygen peaks at energies of approximately 100 eV with

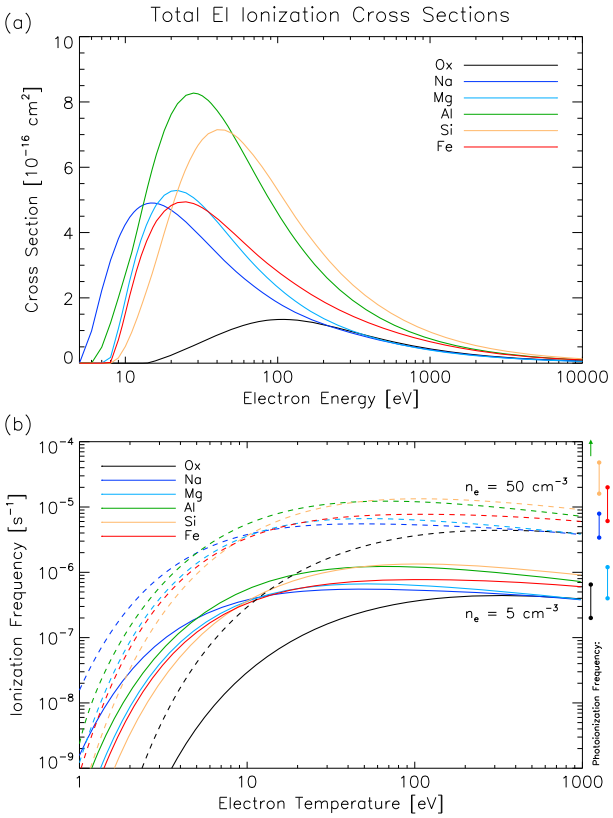

Figure 1. (a) The electron impact ionization cross section as a function of impacting electron energy for all six species modeled in the torus [*Bartlett and Stelbovics*, 2002, 2004]. (b) The ionization frequency as a function of electron temperature for all six selected species in the torus for two example electron densities: (i) $n_e = 5$ cm^{-3} (solid lines) and (ii) $n_e = 50$ cm^{-3} (dashed lines). The corresponding range photo-ionization frequencies at 1.5 AU (solar minimum to solar maximum) are shown as vertical colored bars to the right of the panel. Note that the photo-ionization frequency for Al is off the top of the panel and denoted by the arrow.

a maximum cross section of $\sigma = 10^{-16}$ cm^2. Sodium, magnesium, and iron have EI ionization cross sections nearly 5 times that of oxygen, $\sigma \approx 5 \times 10^{-16}$ cm^2 but centered at much lower energies near 10–20 eV. Silicon and aluminum have the highest EI ionization cross sections of 7×10^{-16} and 8.5×10^{-16} centered at slightly higher energies of 25 and 50 eV, respectively. All cross sections drop to zero for decreasing energies less than ≈10 eV, while maintaining extended tails to 1 keV electron energies and above. Using the cross sections shown in Figure 1a, we can calculate the ionization frequencies (measured in s^{-1}) for various values of the ambient electron temperature and density. We assume a Maxwellian electron distribution and integrate the electron flux over the EI cross sections. Figure 1b shows the result of this calculation for all six species as a function of the Maxwellian electron temperature, for two example densities: (i) $n_e = 5$ cm^{-3} (solid lines) and (ii) $n_e = 50$ cm^{-3} (dashed lines). These densities are roughly representative of the solar wind and Martian magnetosheath, respectively. For electron temperatures between 10 and 100 eV, most ionization frequencies are between 10^{-7} and 10^{-6} s^{-1} for $n_e = 5$ cm^{-3} and between 10^{-6} and 10^{-5} s^{-1} for $n_e = 50$ cm^{-3}. For comparison, we also show the range of photo-ionization frequencies at 1.5 AU (i.e., solar minimum to solar maximum) as corresponding colored bars to the right of Figure 1b [*Huebner and Mukherjee*, 2015]. The relative importance of photo-ionization and electron impact ionization varies significantly by species. At one end, oxygen has a photo-ionization frequency of $\approx 4 \times 10^{-7}$ s^{-1}, higher than electron impact ionization frequencies in the solar wind at $T_e = 10$ eV yet significantly lower than EI ionization frequencies in the Martian magnetosheath, where $T_e \approx 20$–100 eV. In contrast, the photo-ionization frequency of aluminum is on the order of 10^{-3} (off the chart) and, thus, always greater than the EI ionization frequency at Mars. The other species lie between these two end-members, with both photo-ionization and EI ionization playing a role in ionizing the neutral Phobos torus species. Finally, charge exchange (CX) cross sections are estimated for 1 keV protons from the

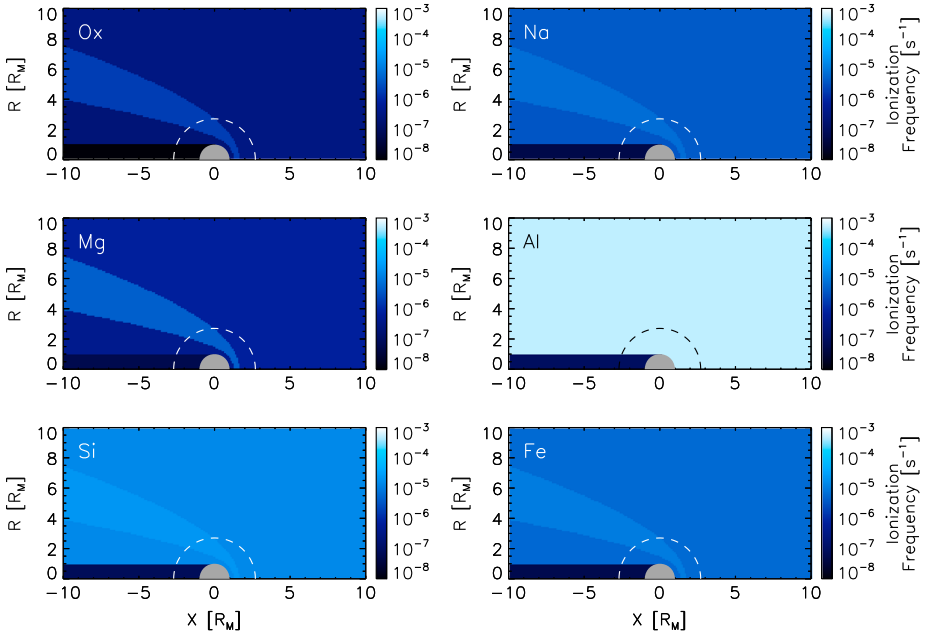

Figure 2. The total ionization frequency (electron impact, charge exchange, and photo-ionization) for all six species as a function of location with respect to Mars (assuming cylindrical symmetry). Phobos' orbit is shown as the dashed line.

following sources: O [*Stebbings et al.*, 1964], Na [*Aumayr et al.*, 1987; *Ebel and Salzborn*, 1987], Mg [*Pandey et al.*, 2007], and Fe [*Rutherford and Vroom*, 1972]. Al and Si are assumed to have identical cross sections as Fe.

To implement the photo-ionization, electron impact ionization, and charge exchange ionization in the neutral Monte Carlo model as a loss term for neutrals, we have adopted a relatively simple model. We set the photo-ionization rates equal to each species' respective solar median rate and apply this rate whenever a neutral atom is sunlit, i.e., not in Mars' optical shadow. For electron impact ionization, we define three plasma regions: (i) the solar wind, (ii) the Martian magnetosheath, and (iii) the Martian magnetotail. The boundaries between these three regions are taken from the statistical study of *Vignes et al.* [2000]. The plasma parameters in each region, which control the EI ionization frequency, are (i) solar wind, $n_e = 5$ cm^{-3}, $T_e = 10$ eV; (ii) Martian magnetosheath, $n_e = 50$ cm^{-3}, $T_e = 50$ eV; and (iii) Martian magnetotail, $n_e = 0.5$ cm^{-3}, $T_e = 20$ eV [see, e.g., *Dubinin et al.*, 2008]. While these boundaries and plasma parameters are necessarily averaged and represent a fairly simple model, they nevertheless capture, to first order, the varying EI ionization frequencies for torus neutrals around Mars. For CX ionization rates, we assume that the solar wind is a 1 keV proton beam with density 5 cm^{-3} and velocity 400 km/s. We assume identical values for use in estimating the magnetosheath CX ionization rate. This may not accurately capture the CX ionization in the shocked, heated, and decelerated magnetosheath plasma; however, this suffices to calculate the CX contribution in the magnetosheath. CX ionization is set to 0 in the magnetotail. Table 1 lists the photo-ionization, electron impact ionization, and charge exchange ionization rates for all species used in the model. Figure 2 shows the total ionization frequency (photo + EI + CX) as a function of position relative to Mars for each species. For all species except Al, variations in the ionization frequency between the solar wind, magnetosheath, magnetotail, and optical shadow are seen. The highest ionization frequencies for these species occur within the magnetosheath where electron impact ionization is at its highest (along with the contributions from photo-ionization and charge exchange). Aluminum, whose photo-ionization frequency is nearly 2 orders of magnitude higher than its EI ionization frequency, has an indistinguishable change in total ionization frequency between the solar wind, magnetosheath, and magnetotail and only drops to its minimum in the optical shadow of Mars, where EI ionization from tail electrons is the only ionization process. Lastly, we emphasize again that these values are average in nature and do not capture the inherent variability, both spatial and temporal, that may alter the total ionization frequencies shown here.

2.3. Neutral Torus Distributions

Figure 3 shows the equilibrium neutral Phobos torus distributions resulting from charged particle sputtering for the six selected species in both the ecliptic (*xy*) and meridional (*yz*) planes. Each case is normalized to its

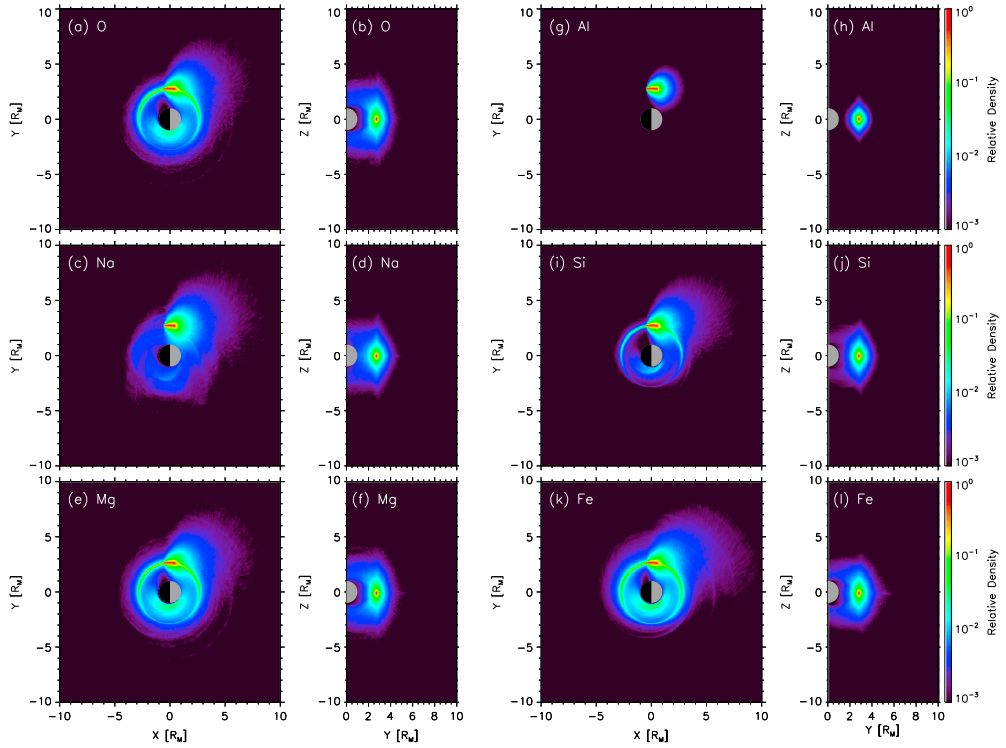

Figure 3. The Phobos torus neutral distributions generated through charged particle sputtering shown in both the ecliptic (*xy*) plane and the meridional (*yz*) plane for (a, b) oxygen, (c, d) sodium, (e, f) magnesium, (g, h) aluminum, (i, j) silicon, and (k, l) iron, respectively. All panels are normalized with respect to their own maximum, for comparison.

own respective maximum, for comparison, and shown for Phobos at dusk. O, Mg, Si, and Fe share a common neutral torus morphology with a maximum at the position of Phobos, a plume of neutrals directed sunward originating directly from Phobos, and a partial, asymmetric, ring-like torus encircling most of Mars. The plumes originating from Phobos are due to freshly ejected neutrals that have velocities near or above the requisite Martian escape velocity. In contrast, the ring-like structure is formed by neutrals ejected from Phobos that have velocities at or below Martian escape velocity and, thus, remain bound in orbit around Mars. The asymmetric nature of the torus between the dawnside and duskside of Mars is due to the addition or subtraction of Phobos' orbital velocity (≈2 km/s) to the sputtered neutral velocity distribution. At dusk, Phobos' orbital motion is antisunward, and thus, neutrals ejected from the dayside of Phobos are decelerated in the Martian frame and, thus, are more likely to be bound to Mars. At dawn, Phobos' orbital motion is sunward, and sputtered neutral velocities are added to Phobos' velocity such that the sputtered velocity distribution contains a higher fraction above escape velocity. Differences in the thickness of the torus by species are due to both differing initial ejection velocity distributions and the varying ionization timescales across species. Na neutrals possess a plume of freshly ejected particles similar to that of the previous species; however, solar radiation pressure distorts and diffuses any ring- or torus-like structure. Finally, the Al neutral torus is unique among the species modeled. Due to the relatively short photo-ionization lifetime of Al relative to the mean orbital period, the Al neutrals do not form a torus encircling Mars but rather a very limited corona around the instantaneous position of Phobos. The meridional distribution for all species peaks at the location of Phobos ($y = +2.7\,R_M$), declines moderately inward of the orbit of Phobos toward Mars, and declines sharply outside of the orbit of Phobos. The neutral distributions extend several Martian radii in height above and below the Phobos orbital plane. Smaller differences in the vertical extent of the neutral torus between different species are due to both the differing masses between species and differing ionization timescales.

Figure 4 shows the neutral torus distributions for micrometeoroid impact vaporization in the same format as Figure 3. O, Mg, Si, and Fe have similar distributions, with a full, nearly isotropic torus formed around Mars and a local maximum at the position of Phobos. The Na distribution for MIV neutrals is complex, reflecting the role that solar radiation pressure plays in distorting the individual neutral trajectories. The distorted Na neutral distribution is analogous to observations of solar radiation-induced perturbations of Na clouds at Earth's

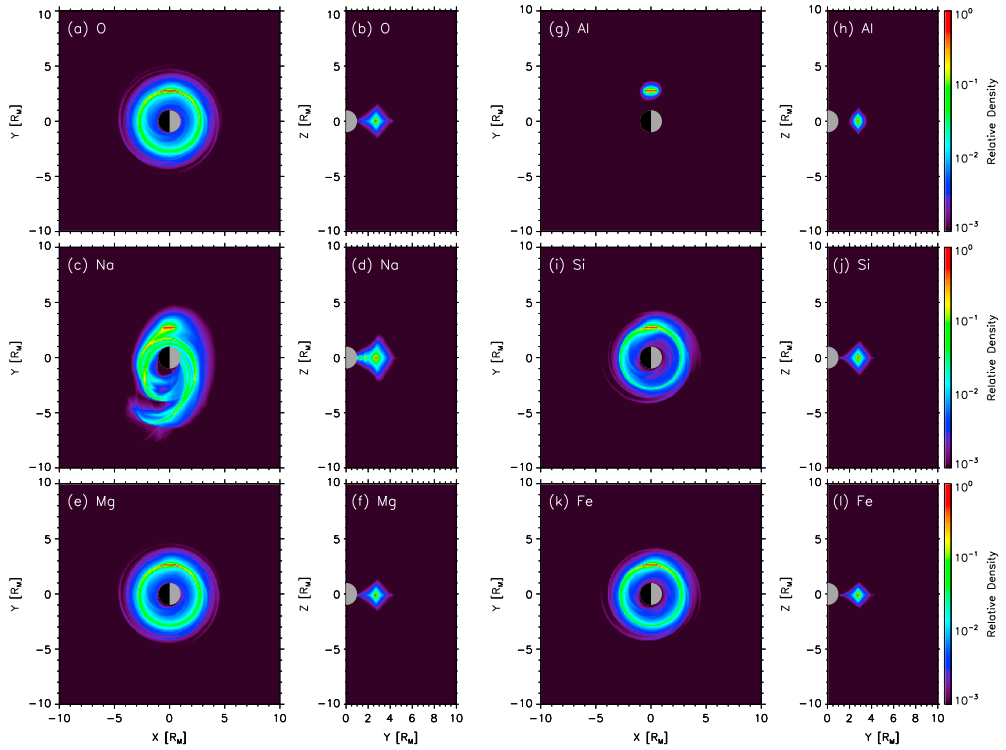

Figure 4. The Phobos torus neutral distributions generated through micrometeoroid impact vaporization in the same format as Figure 3.

Moon [e.g., *Mendillo et al.*, 1997; *Lee et al.*, 2011], comets [e.g., *Cremonese et al.*, 1997], and the Jovian system [e.g., *Smyth and Combi*, 1988; *Smyth*, 1992; *Burger and Johnson*, 2004]. Finally, similar to the sputtered neutral distribution, Al neutrals form a small coma around the instantaneous position of Phobos itself. We note that the lower temperature of vaporized material relative to sputtered neutrals implies that very little of the material is lost from the torus due to either ballistic escape from the Martian system or infall into Mars' atmosphere. Thus, the main escape channel for torus neutrals produced through micrometeorite impact vaporization is ionization and loss to the solar wind or Martian magnetosphere.

In addition to the relative densities shown in Figures 3 and 4, we can estimate the absolute density of each neutral species within the torus. For sputtering, we use the orbit-averaged neutral production rates calculated by *Poppe and Curry* [2014], who estimated a total production rate of $Q_{sp} = 1.5\text{–}6 \times 10^{19}$ s^{-1}. For the calculations here, we use an intermediate value of $Q_{sp} = 3 \times 10^{19}$ s^{-1}, noting the degree of variability expected from both the solar wind and Martian planetary ion outflux. Micrometeorite impact vaporization will also contribute; however, *Cipriani et al.* [2011] has estimated that MIV production is roughly 2 orders of magnitude smaller than surface sputtering ($Q_{MIV} \sim 10^{17}$ s^{-1}); thus, we neglect the MIV contribution further in this study (although we do note that significant enhancements may occur during meteor showers [i.e., *Christou*, 2004, 2010]). Extrapolating calculations performed for Earth's Moon [*Sarantos et al.*, 2012], we calculate a Na PSD generation rate of 2.7×10^{18} Na atoms s^{-1}. Using the number fraction of each species present in the regolith, the fractional production rate for each

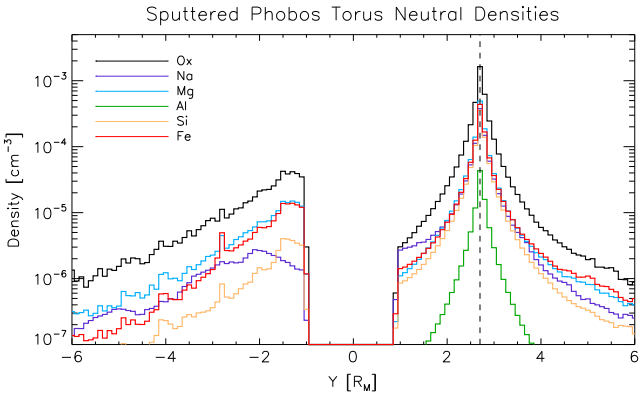

Figure 5. The density of sputtered Phobos torus neutrals for all six species along the *y* axis. Phobos is located at $y = +2.7\,R_M$ (i.e., dusk) at the dashed line.

species can be calculated, listed in Table 1. Figure 5 shows the absolute density of each neutral species as a function of distance along the y axis in the Phobos orbital plane with Phobos located at dusk, $y = +2.7$ R_M (vertical dashed line). Oxygen is the dominant component of the neutral torus with a maximum density near Phobos of 1.6×10^{-3} cm^{-3}. Sodium, magnesium, silicon, and iron have nearly equivalent densities in the torus near Phobos, with maxima of approximately $4-5 \times 10^{-4}$ cm^{-3}. Finally, aluminum has the smallest density with a maximum of approximately 4.3×10^{-5} cm^{-3}. These densities are comparable to those found in earlier simulations [*Cipriani et al.*, 2011], and thus, we reach a similar conclusion that in situ neutral mass spectrometers are unable to measure the putative Phobos torus in neutral form. Such small densities are more likely to be measured in their ionized form by charged particle detectors (i.e., see *Halekas et al.* [2015] for measurements of lunar pickup ions using the ion mode from a neutral mass spectrometer).

3. Phobos Pickup Ions

3.1. Hybrid Plasma Model

In order to define the flux of Phobos torus pickup ions within the Martian system, we require the background magnetic and electric fields. The electromagnetic fields within the Martian magnetosphere are calculated by a hybrid plasma model (particle ions/fluid electrons), previously used to study objects such as the Moon both globally and regionally [e.g., *Holmström et al.*, 2012; *Fatemi et al.*, 2015], Mars [*Holmström and Wang*, 2015], and the outer planet moons [*Lindkvist et al.*, 2015]. While the details of the hybrid model are described in *Holmström* [2013], we briefly discuss the specific application of the model for Mars used here. In order to adapt the hybrid model for Mars, we have included a cold, outflowing ionospheric plasma source consisting of planetary O^+ ions. We do not include the presence of Martian crustal fields because we wish only to capture the gross morphology of the Martian magnetosphere and are not pursuing a detailed study of ionospheric or magnetospheric physics at Mars. Variations in ionospheric outflow at Mars can impact the structure of the Martian magnetosphere downstream from the planet, potentially affecting the magnetic and electric field structure at the orbit of Phobos downstream, yet a full investigation of this variability is beyond the scope of the current paper. The model uses a domain of $12 \times 17 \times 17$ R_M with a 400 km (0.118 R_M) grid cell size. We use standard solar wind parameters at Mars' orbital distance, with density 4.0 cm^{-3}, flow speed 400 km/s, ion and electron temperatures of 50,000 K (4.3 eV) and 140,000 K (12.0 eV), respectively, and an alpha-to-proton density ratio of 0.05. We ran two cases for the interplanetary magnetic field configuration: Parker spiral with $B = [2.1, 2.1, 0]$ nT and B_z with $B = [0, 0, 5.0]$ nT. The model possesses a Chapman profile for atmospheric ions (O^+ only) with a total ion production rate of 5×10^{24} s^{-1}, atmospheric scale height of 250 km, and cosine solar zenith angle distribution, all of which are consistent with previous work [e.g., *Fox and Haćic*, 1997; *Chaufray et al.*, 2007; *Valeille et al.*, 2009].

Figure 6 shows the density, bulk velocity, magnetic field magnitude, and electric field magnitude, respectively, in the ecliptic plane (xy) for the B_z case from the hybrid model. The structure of the Martian magnetosphere is clearly seen, with a bow shock, magnetosheath, and magnetotail all well formed, in agreement with many other models of the Mars-solar wind interaction [*Brain et al.*, 2010, and references therein]. The dotted line in each panel denotes the approximate location of the Martian bow shock as best fit to the hybrid model results using the axisymmetric function derived by *Vignes et al.* [2000], namely, $r = L/(1 + \epsilon \cos\theta)$, measured from the focus $x = X_O$, where r and θ are the standard cylindrical coordinates, and L and ϵ are the semilatus rectum and eccentricity, respectively. Fits to Mars Global Surveyor data yielded an average set of fit parameters, $\{X_O, L, \epsilon\} = \{0.64, 2.04, 1.03\}$, while the best fit determined for this hybrid simulation run yielded slightly different parameters of $\{X_O, L, \epsilon\} = \{0.90, 2.13, 1.10\}$. With these parameters, the *Vignes et al.* [2000] function fits the bow shock surface reasonably well, noting some asymmetry between the dawn and dusk flanks of the bow shock (most likely induced by the inherent asymmetry of the convection electric field). The slight difference between the parameters derived for our hybrid simulation run and the average *Vignes et al.* [2000] parameters is best understood in light of the average nature of the MGS results versus the single hybrid model result shown here. The bow shock location is most likely a function of the ionospheric production rate, the solar wind pressure, and the IMF orientation. Finally, we also note the multiple shock structure along the dusk flank of the magnetosphere in these results; such a structure has been previously observed in other hybrid simulations [e.g., *Burgess*, 1989; *Shimazu*, 2001; *Brain et al.*, 2010].

3.2. Torus Pickup Ion Distributions

To determine the density and flux of torus pickup ions, we used the results of the neutral torus Monte Carlo model and the electromagnetic fields from the hybrid model (Figure 6) as input to a particle tracing model.

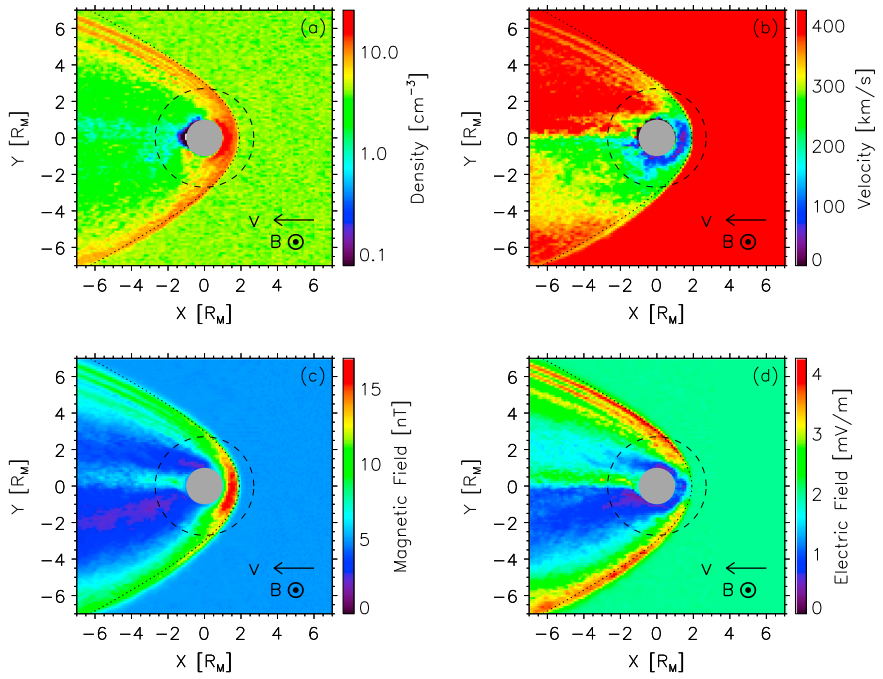

Figure 6. The (a) density, (b) velocity, (c) magnetic field, and (d) convection electric field in the Martian magnetosphere from the plasma hybrid model for the B_z case. The Parker spiral results are qualitatively similar with different directions for the magnetic and electric fields (not shown). The orbit of Phobos is shown as the dashed line, and the solar wind velocity and IMF direction are denoted in each panel. The dotted line shows the approximate location of the bow shock fit to the model of *Vignes et al.* [2000] for this simulation (see text for full discussion).

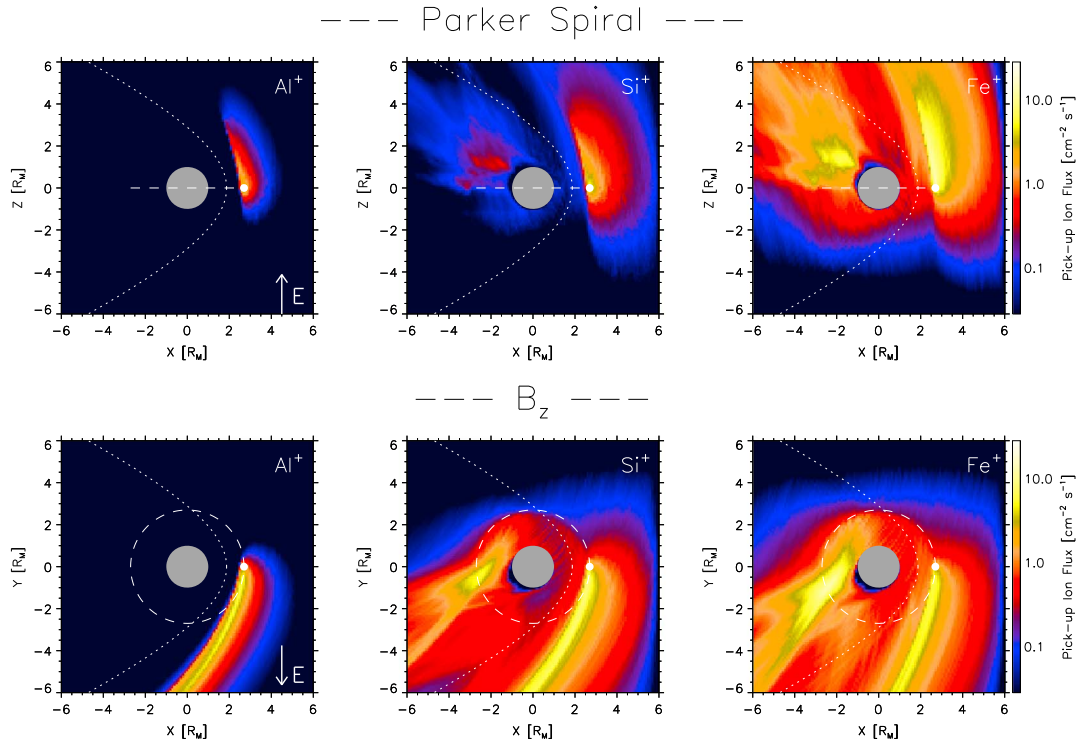

Figure 7. (top row) The pickup ion flux for Al^+, Si^+, and Fe^+, respectively, for Parker spiral IMF. (bottom row) The pickup ion flux for Al^+, Si^+, and Fe^+, respectively, for B_z IMF. The orbit of Phobos is shown by the dashed line, and the instantaneous position of Phobos is at Martian noon. The electric field direction for each case is shown in the lower right corner of the Al^+ panel. The location of the Martian magnetospheric bow shock as determined from the hybrid model is denoted in each panel by the dotted curve.

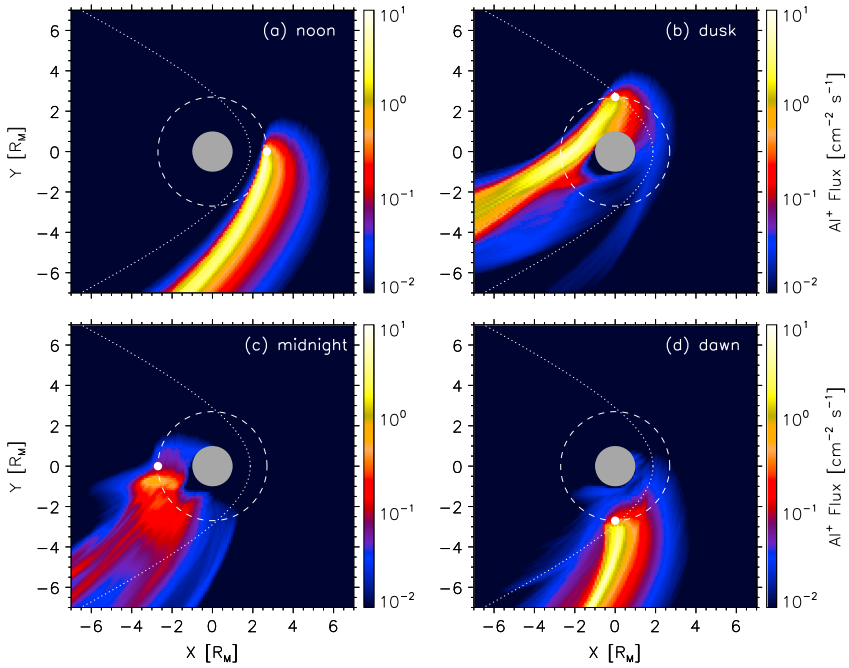

Figure 8. The Al^+ pickup ion flux from the Phobos torus in the ecliptic plane for varying local time positions of Phobos under B_z IMF conditions. The orbit of Phobos is shown by the dashed line, and the instantaneous position of Phobos is shown as the solid white dot. The location of the Martian magnetospheric bow shock as determined from the hybrid model is denoted in each panel by the dotted curve.

The ion tracing model tracks the trajectory of pickup ions born from the Phobos torus through the electromagnetic environment of Mars' magnetosphere. For each species, ions are initialized throughout a sphere of $6R_M$ surrounding Mars and assigned a weight according to the total ionization rate (i.e., neutral density times ionization frequency) at that location for each species. At every time step, each ion is advanced according to the Lorentz force using a fourth-order Runge-Kutta algorithm with electromagnetic fields interpolated from the hybrid grid to the instantaneous position of the ion. Each ion is tracked until it either intersects Mars or escapes from the simulation domain entirely. For each species, we traced 5×10^6 particles and recorded their position and velocity on a $14 \times 16 \times 16$ R_M grid with $0.1R_M$ grid spacing for calculation of the density and isotropic flux.

Figure 7 shows the flux for Al^+, Si^+, and Fe^+ pickup ions from the Phobos torus for the two IMF configurations, Parker spiral and B_z, with Phobos located at noon local time. The Parker Spiral case is shown in Figure 7 (top row) as a cut in the xz plane at $y = 0$, while the B_z case is shown in Figure 7 (bottom row) as a cut in the xy plane at $z = 0$. In the Parker spiral case, torus pickup ions are accelerated northward from the torus along the interplanetary and magnetospheric electric field. The highest concentrations of Al^+ fluxes are found just northward of Phobos, corresponding to the concentration of neutral Al near Phobos (see Figure 3g). Both Si^+ and Fe^+ ions have much more extended fluxes due to the fully populated neutral torus for these species (Figures 3i and 3k, respectively). For B_z IMF conditions, shown in Figure 7 (bottom row), torus pickup ions are mainly confined to the Phobos orbital plane as the electric field is generally in the y direction. Ions born in the solar wind (i.e., outside the Martian bow shock) follow classical $E \times B$ pickup trajectories and are quickly convected away from Mars. Al^+ ions remain fully outside the Martian magnetosphere while Phobos is at noon, while the Si^+ and Fe^+ ions, which originate from broad torus neutral distributions, have a significant amount of flux inside the magnetosphere. This flux originates from both ions generated within the magnetosphere and also ions that have been generated "upstream" of the magnetosphere (in the sense along the electric field) and have been accelerated into and across the magnetotail. Maximum fluxes for these species in the B_z case are nearly identical to those in the Parker spiral case. The absolute pickup ion flux for each species has also been calculated using the neutral densities shown in Figure 5 and the total ionization rates. Al^+, Si^+, and Fe^+ pickup ions have maximum fluxes of approximately 6, 10, and 14 cm^{-2} s^{-1}, respectively. Maximum fluxes for all species are listed in Table 1, with a total maximum flux summed over species of ≈200 cm^{-2} s^{-1}.

The distribution of torus pickup ions is also determined by the instantaneous position of Phobos about its orbit. Figure 8 shows the flux of Al^+ pickup ions in the Phobos orbital plane for the B_z IMF case only but for selected positions of Phobos along its orbit: (a) noon, (b) dusk, (c) midnight, and (d) dawn. For comparison, Figure 8a reproduces the Al^+ pickup ion flux presented earlier in Figure 7, with a concentrated beam of ions following classical $E \times B$ pickup trajectories out of the Martian system. In Figure 8b, Phobos has moved a quarter of the way around its orbit. Here most Al^+ pickup ions are generated just inside the Martian bow shock and are convected down and across the Martian magnetotail. Some fraction of these ions are accelerated into the Martian ionosphere and atmosphere and, similar to Martian planetary pickup ions (typically O^+), may play a role in sputtering the Martian atmosphere and inducing atmospheric loss [e.g., *Luhmann and Kozyra*, 1991; *Leblanc et al.*, 2015]. These Al^+ ions, along with other metallic species originating from Phobos, will eventually neutralize in the atmosphere of Mars and represent a source of metals in the upper atmosphere, in addition to metal ions and neutrals deposited from meteoric ablation [e.g., *Molina-Cuberos et al.*, 2003]. We note that the other torus species (i.e., Fe, Mg, and Si) will also contribute to metallic fluxes to the atmosphere of Mars over a larger range of Phobos local times given that their neutral distributions are much broader than that for Al. In Figure 8c, Phobos is located at midnight and the total ionization rate is significantly lower since most of the neutral Al cloud is in shadow (see Figure 2). The overall magnitude of Al^+ fluxes at this time is lower than that at other times when Phobos and the neutral Al cloud are in sunlight. The ions that are produced are convected cross tail and down tail and lost from the Martian system. Finally, Figure 8d shows the pickup ion flux at dawn. Similar to the results at noon, Figure 8a, the Al^+ ions are mainly born in the solar wind and quickly convected away.

4. Discussion and Conclusion

The models presented here have quantified the neutral and ionized torus generated from the interaction of Phobos with its ambient plasma environment given knowledge of relevant processes gained from the study of other airless bodies in the inner solar system. Phobos' neutral torus is mainly produced through solar wind sputtering of surface material, and thus, the composition of the torus reflects the surface composition of Phobos. Assuming a typical D-type asteroidal surface composition [*Rivkin et al.*, 2002], dominant species include oxygen, magnesium, iron, aluminum, silicon, and sodium. The neutral Monte Carlo model demonstrates that most of these species should form fully populated tori in orbit around Mars concentric with Phobos' orbit. Aluminum, as an exception, has a relatively short photo-ionization lifetime of approximately 30 min, and Al neutrals are ionized and lost to the solar wind or Martian magnetosphere before extending fully in orbit around Mars. Subtler differences in the neutral distributions between torus species are ascribed to both differing ionization lifetimes and ejection velocity distributions. The overall density of the Phobos torus is estimated to be very low, $<10^{-2}$ cm^{-3} in total across all species, presenting an extreme challenge for in situ neutral measurements.

Our neutral model can be compared with previous estimates for the structure and density of the Phobos torus. *Mura et al.* [2002] modeled the torus as produced from active outgassing of oxygen from Phobos (as proposed by *Fanale and Salvail* [1989]). The estimated rate of outgassing, $Q \approx 10^{23}$ s^{-1}, and an assumed neutral temperature of 250K combined to produce a narrow and dense torus encircling Mars with peak neutral densities on the order of 10^5 cm^{-3}. This torus is distinctly different from that derived here, as our production rate is nearly 4 orders of magnitude lower and the neutral emission temperature (due to either sputtering, micrometeorite vaporization, or photon-stimulated desorption) is between 1 and 2 orders of magnitude larger. Thus, the torus modeled here has a much larger spatial extent and is much more tenuous. The composition of the torus is also important to consider; whereas *Mura et al.* [2002] considered only oxygen from direct outgassing, the torus we model includes refractory elements (Na, Mg, Al, Si, and Fe) directly liberated from the Phobos regolith. Our torus model is much closer to that predicted by *Cipriani et al.* [2011], who considered solar wind sputtering only. The neutral densities derived by *Cipriani et al.* [2011] near Phobos are within an order of magnitude of the maximum neutral densities predicted here for O, Na, Mg, Al, and Fe; *Cipriani et al.* [2011] did not model Si. The spatial distributions of Mg, O, and Fe do differ between the two models [see *Cipriani et al.*, 2011, Figure 4] with our model forming a more distinct torus-like structure for most species as opposed to a broader cloud seen in *Cipriani et al.* [2011].

The ionized component of the Phobos torus is continuously present throughout the Martian system as torus neutrals are ionized and picked up by ambient electric and magnetic fields. In the solar wind, these newly born

ions follow classical $E \times B$ trajectories similar to that at the Moon [i.e., *Halekas et al.*, 2012], while pickup ions that are either born within or enter the Martian magnetosphere have more complex trajectories. Generally, the maximum pickup ion fluxes are very low across all species, with fluxes ranging from 125 cm^{-2} s^{-1} for oxygen to 6.0 cm^{-2} s^{-1} for aluminum. As noted earlier, oxygen pickup ions from the Phobos torus will be indistinguishable from the Martian coronal oxygen pickup ions, and thus, the net maximum flux of metallic species that could be confidently attributed to Phobos is on the order of 75 cm^{-2} s^{-1}. Clearly, this flux is very low and does not represent a sufficient enough flux to locally perturb the solar wind or Martian magnetosphere, consistent with the nondetection of any such plasma perturbations correlated with the orbit of Phobos [*Øieroset et al.*, 2010]. Indeed, such low fluxes are not likely to be detected with in situ instrumentation such as that found on the Mars Atmosphere and Volatile Evolution (MAVEN) mission [*Jakosky et al.*, 2014] under the nominal conditions studied here. Extreme conditions, such as interplanetary coronal mass ejections (ICMEs) or solar flares, may enhance both surface sputtering and photo-ionization [e.g., *Dong et al.*, 2015; *Jakosky et al.*, 2015], resulting in a denser neutral torus and greater flux of Phobos pickup ions. Studies of the effects of ICMEs on the lunar exosphere have predicted increases in exospheric densities of over an order of magnitude shortly after the passage of the ICME past the Moon [*Killen et al.*, 2012], and analogous conclusions most likely apply to Phobos as well.

The search for the Phobos torus has spanned several decades, yet even in the absence of any direct detection of the torus, our knowledge has steadily increased. We know that contrary to early suggestions [*Fanale and Salvail*, 1989], Phobos is an inert object and not cryovolcanically active. It has also been shown that the perturbations of the Martian environment induced by the presence of Phobos must be exceedingly small [e.g., *Øieroset et al.*, 2010], a conclusion that aligns with the low neutral and ionized densities predicted here for the torus. Nevertheless, future detection of Phobos-induced phenomena, whether from the moon itself or from a torus of sputtered or vaporized neutrals, would enable a significant step in our understanding of such a small moon and further our understanding of possible exospheres at other small bodies and asteroids throughout the solar system [e.g., *Morgan and Killen*, 1998; *Schläppi et al.*, 2008; *Morse et al.*, 2012]. Such findings would hopefully include a measure of the elemental surface composition of Phobos, a measurement that may help to constrain both the various theories for the origin of both Phobos and Deimos and the role of ongoing surface modification processes at Phobos, especially in the light of the remarkable color heterogeneity on the surface of Phobos [e.g., *Murchie et al.*, 1991; *Murchie and Erard*, 1996]. We hope that the models presented here serve both as a guide for searching for the Phobos torus and as a tool for correctly interpreting any such observations.

Acknowledgments
A.R.P. and S.F. gratefully acknowledge support from NASA's Solar System Exploration Research Virtual Institute (SSERVI), grant NNX14AG16A. S.M.C. acknowledges support from the Mars Atmosphere and Volatile EvolutioN (MAVEN) mission. The authors thank J.G. Luhmann for constructive discussions. Data from the modeling results are available upon request to A.R.P. The authors thank three reviewers for constructive comments that greatly improved the paper.

References

Altwegg, K., et al. (2012), In situ mass spectrometry during the Lutetia flyby, *Planet. Space Sci.*, *66*, 173–178.
Aumayr, F., G. Lakits, and H. Winter (1987), Charge transfer and target excitation in H^+-Na(3s) collisions (2–20 keV), *J. Phys. B At. Mol. Opt. Phys.*, *20*, 2025–2030.
Bartlett, P. L., and A. T. Stelbovics (2002), Calculation of electron-impact total-ionization cross sections, *Phys. Rev. A*, *66*, 012707.
Bartlett, P. L., and A. T. Stelbovics (2004), Electron-impact ionization cross sections for elements $Z = 1$ to $Z = 54$, *At. Data Nucl. Data Tables*, *86*, 235–265.
Benna, M., P. R. Mahaffy, J. S. Halekas, R. C. Elphic, and G. T. Delory (2015), Variability of helium, neon, and argon in the lunar exosphere as observed by the LADEE NMS instrument, *Geophys. Res. Lett.*, *42*, 3723–3729, doi:10.1002/2015GL064120.
Biersack, J. P., and W. Eckstein (1984), Sputtering studies with the Monte Carlo program TRIM.SP, *Appl. Phys. A*, *34*, 73–94.
Brain, D., et al. (2010), A comparison of global models for the solar wind interaction with Mars, *Icarus*, *206*, 139–151.
Burger, M. H., and R. E. Johnson (2004), Europa's neutral cloud: Morphology and comparisons to Io, *Icarus*, *171*, 557–560.
Burgess, D. (1989), Cyclic behavior at quasi-parallel collisionless shocks, *Geophys. Res. Lett.*, *16*(5), 345–348.
Carlson, R. W. (1999), A tenuous carbon dioxide atmosphere on Jupiter's Moon Callisto, *Science*, *283*, 820–821.
Chaufray, J. Y., R. Modolo, F. Leblanc, G. Chanteur, R. E. Johnson, and J. G. Luhmann (2007), Mars solar wind interaction: Formation of the Martian corona and atmospheric loss to space, *J. Geophys. Res.*, *112*, E09009, doi:10.1029/2007JE002915.
Christou, A. A. (2004), Predicting Martian and Venusian meteor shower activity, *Earth Moon Planets*, *95*, 425–431.
Christou, A. A. (2010), Annual meteor showers at Venus and Mars: Lessons from the Earth, *Mon. Not. R. Astron. Soc.*, *402*, 2759–2770.
Cipriani, F., O. Witasse, F. Leblanc, R. Modolo, and R. E. Johnson (2011), A model of interaction of Phobos' surface with the Martian environment, *Icarus*, *212*, 643–648.
Citron, R. I., H. Genda, and S. Ida (2015), Formation of Phobos and Deimos via a giant impact, *Icarus*, *252*, 334–338.
Craddock, R. A. (2011), Are Phobos and Deimos the result of a giant impact?, *Icarus*, *211*, 1150–1161.
Cremonese, G., H. Boehnhardt, J. Crovisier, H. Rauer, A. Fitzsimmons, M. Fulle, J. Licandro, D. Pollacco, G. P. Tozzi, and R. M. West (1997), Neutral sodium from comet Hale-Bopp: A third type of tail, *Astrophys. J.*, *490*, L199–L202.
Cunningham, N. J., J. R. Spencer, P. D. Feldman, D. F. Strobel, K. France, and S. N. Osterman (2015), Detection of Callisto's oxygen atmosphere with the Hubble Space Telescope, *Icarus*, *254*, 178–189.
Dong, C., et al. (2015), Multifluid MHD study of the solar wind interaction with Mars' upper atmosphere during the 2015 March 8th ICME event, *Geophys. Res. Lett.*, *42*, 9103–9112, doi:10.1002/2015GL065944.

Dubinin, E., et al. (2008), Plasma environment of Mars as observed by simultaneous MEX-ASPERA-3 and MEX-MARSIS observations, *J. Geophys. Res.*, *113*, A10217, doi:10.1029/2008JA013355.
Dubinin, E. M., N. F. Pissarenko, S. V. Barabash, A. V. Zakharov, R. Lundin, R. Pellinen, and K. Schwingenschuh (1991), Plasma and magnetic field effects associated with Phobos and Deimos tori, *Planet. Space Sci.*, *39*(1/2), 113–21.
Ebel, F., and E. Salzborn (1987), Charge transfer of 0.2–5.0 keV protons and hydrogen atoms in sodium-, potassium-, and rubidium-vapour targets, *J. Phys. B At. Mol. Opt. Phys.*, *20*, 4531–4542.
Eichhorn, G. (1976), Analysis of the hypervelocity impact process from impact flash measurements, *Planet. Space Sci.*, *24*, 771–781.
Fanale, F. P., and J. R. Salvail (1989), Loss of water from Phobos, *Geophys. Res. Lett.*, *16*(4), 287–290.
Fatemi, S., C. Lue, M. Holmström, A. R. Poppe, M. Wieser, S. Barabash, and G. T. Delory (2015), Solar wind plasma interaction with Gerasimovich lunar magnetic anomaly, *J. Geophys. Res. Space Physics*, *120*, 4719–4735, doi:10.1002/2015JA021027.
Feldman, P. D., M. A. McGrath, D. F. Strobel, H. W. Moos, K. D. Retherford, and B. C. Wolven (2000), HST/STIS ultraviolet imaging of polar aurora on Ganymede, *Astrophys. J.*, *535*, 1085–1090.
Feldman, P. D., et al. (2012), Temporal variability of lunar exospheric helium during January 2012 from LRO/LAMP, *Icarus*, *221*, 854–858.
Fox, J. L., and A. Hać (1997), Spectrum of hot O at the exobases of the terrestrial planets, *J. Geophys. Res.*, *102*(A11), 24,005–24,011.
Futaana, Y., S. Barabash, M. Holmström, A. Fedorov, H. Nilsson, R. Lundin, E. Dubinin, and M. Fränz (2010), Backscattered solar wind protons by Phobos, *J. Geophys. Res.*, *115*, A10213, doi:10.1029/2010JA015486.
Halekas, J. S., A. R. Poppe, G. T. Delory, M. Sarantos, W. M. Farrell, V. Angelopoulos, and J. P. McFadden (2012), Lunar pickup ions observed by ARTEMIS: Spatial and temporal distribution and constraints on species and source locations, *J. Geophys. Res.*, *117*, E06006, doi:10.1029/2012JE004107.
Halekas, J. S., M. Benna, P. R. Mahaffy, R. C. Elphic, A. R. Poppe, and G. T. Delory (2015), Detections of lunar exospheric ions by the LADEE neutral mass spectrometer, *Geophys. Res. Lett.*, *42*, 5162–5169, doi:10.1002/2015GL064746.
Hall, D. T., D. F. Strobel, P. D. Feldman, M. A. McGrath, and H. A. Weaver (1995), Detection of an oxygen atmosphere on Jupiter's moon Europa, *Nature*, *373*, 677–679.
Hartmann, W. K. (1987), A satellite-asteroid mystery and a possible early flux of scattered C-class asteroids, *Icarus*, *71*, 57–68.
Hoffman, J. H., R. R. Hodges Jr., F. S. Johnson, and D. E. Evans (1973), Lunar atmospheric composition results from Apollo 17, in *Proceedings of the 4th Lunar Science Conference, Houston, Tex., 5–8 Mar.*, vol. 3, pp. 2865–2875, Pergamon Press, New York.
Holmström, M. (2013), Handling vacuum regions in a hybrid plasma solver, in *Numerical Modeling of Space Plasma Flows (ASTRONUM 2012)*, vol. 474, edited by N. V. Pogorelov, E. Audit, and G. P. Zank, pp. 202–207, Astron. Soc. Pac., San Francisco, Calif.
Holmström, M., and X.-D. Wang (2015), Mars as a comet: Solar wind interaction on a large scale, *Planet. Space Sci.*, *119*, 43–47.
Holmström, M., S. Fatemi, Y. Futaana, and H. Nilsson (2012), The interaction between the Moon and the solar wind, *Earth Planets Space*, *64*, 237–245.
Huebner, W. F., and J. Mukherjee (2015), Photoionization and photodissociation rates in solar and blackbody radiation fields, *Planet. Space Sci.*, *106*, 11–45.
Ip, W.-H., and M. Banaszkiewicz (1990), On the dust/gas tori of Phobos and Deimos, *Geophys. Res. Lett.*, *17*(6), 857–860.
Jakosky, B., et al. (2014), The 2013 Mars Atmosphere and Volatile Evolution (MAVEN) mission to Mars, *Space Sci. Rev.*, *195*(1), 3–48
Jakosky, B. M., et al. (2015), MAVEN observations of the response of Mars to an interplanetary coronal mass ejection, *Science*, *350*, 6261.
Killen, R. M., D. M. Hurley, and W. M. Farrell (2012), The effect on the lunar exosphere of a coronal mass ejection passage, *J. Geophys. Res.*, *117*, E00K02, doi:10.1029/2011JE004011.
Leblanc, F., et al. (2015), Mars heavy ion precipitating flux as measured by Mars Atmosphere and Volatile Evolution, *Geophys. Res. Lett.*, *42*, 9135–9141, doi:10.1002/2015GL066170.
Lee, D.-W., S. J. Kim, D.-H. Lee, H. Jin, and K.-S. Kim (2011), Three-dimensional simulations of the lunar sodium exosphere and its tail, *J. Geophys. Res.*, *116*, A07213, doi:10.1029/2011JA016451.
Lindkvist, J., M. Holmström, K. K. Khurana, S. Fatemi, and S. Barabash (2015), Callisto plasma interactions: Hybrid modeling including induction by a subsurface ocean, *J. Geophys. Res. Space Physics*, *120*, 4877–4889, doi:10.1002/2015JA021212.
Luhmann, J. G., and J. U. Kozyra (1991), Dayside pickup oxygen ion precipitation at Venus and Mars: Spatial distributions, energy deposition and consequences, *J. Geophys. Res.*, *96*(A4), 5457–5467.
McClintock, W. E., E. T. Bradley, R. J. Vervack Jr, R. M. Killen, A. L. Sprague, N. R. Izenberg, and S. C. Solomon (2008), Mercury's exosphere: Observations during MESSENGER's first Mercury flyby, *Science*, *321*, 92–94.
Mendillo, M., J. Emery, and B. Flynn (1997), Modeling the Moon's extended sodium clouds as a tool for investigating sources of transient atmospheres, *Adv. Space Res.*, *19*(10), 1577–1586.
Molina-Cuberos, G. J., O. Witasse, J.-P. Lebreton, R. Rodrigo, and J. J. López-Moreno (2003), Meteoric ions in the atmosphere of Mars, *Planet. Space Sci.*, *51*, 239–249.
Morgan, T. H., and R. M. Killen (1998), Production mechanisms for faint but possibly detectable coronae about asteroids, *Planet. Space Sci.*, *46*(8), 843–850.
Morse, A. D., et al. (2012), The Rosetta campaign to detect an exosphere at Lutetia, *Planet. Space Sci.*, *66*, 165–172.
Mura, A., A. Milillo, S. Orsini, E. Kallio, and S. Barabash (2002), Energetic neutral atoms at Mars: 2. Imaging of the solar wind-Phobos interaction, *J. Geophys. Res.*, *107*(A10), 1278, doi:10.1029/2001JA000328.
Murchie, S., and S. Erard (1996), Spectral properties and heterogeneity of Phobos from measurements by Phobos 2, *Icarus*, *123*, 63–86.
Murchie, S. L., et al. (1991), Color heterogeneity of the surface of Phobos: Relationships to geologic features and comparison to meteorite analogs, *J. Geophys. Res.*, *96*(B4), 5925–5945.
Øieroset, M., D. A. Brain, E. Simpson, D. L. Mitchell, T. D. Phan, J. S. Halekas, R. P. Lin, and M. H. Acuña (2010), Search for Phobos and Deimos gas/dust tori using in situ observations from Mars Global Surveyor MAG/ER, *Icarus*, *206*, 189–198.
Pajola, M., M. Lazzarin, C. M. Dalle Ore, D. P. Cruikshank, T. L. Roush, S. Magrin, I. Bertini, F. La Forgia, and C. Barbieri (2013), Phobos as a D-type captured asteroid, spectral modeling from 0.25 to 4.0 μm, *Astrophys. J.*, *777*, 127.
Pandey, M. K., R. K. Dubey, and D. N. Tripathi (2007), Charge exchange collisions of H^+/D^+ ions with alkaline Earth atoms (Ca, Mg), *Eur. Phys. J. D*, *41*, 275–279.
Pollack, J. B., J. A. Burns, and M. E. Tauber (1979), Gas drag in primordial circumplanetary envelopes: A mechanism for satellite capture, *Icarus*, *37*, 587–611.
Poppe, A. R., and S. M. Curry (2014), Martian planetary heavy ion sputtering of Phobos, *41*, 6335–6341, doi:10.1002/2014GL061100
Potter, A. E., and T. H. Morgan (1985), Discovery of sodium in the atmosphere of Mercury, *Science*, *229*, 651–653.
Potter, A. E., and T. H. Morgan (1986), Potassium in the atmosphere of Mercury, *Icarus*, *67*, 336–340.
Rivkin, A. S., R. H. Brown, D. E. Trilling, J. F. Bell III, and J. H. Plassmann (2002), Near-infrared spectrophotometry of Phobos and Deimos, *Icarus*, *156*, 64–75.

Rodríguez, D. F., L. Saul, P. Wurz, S. A. Fuselier, H. O. Funsten, D. J. McComas, and E. Möbius (2012), IBEX-Lo observations of energetic neutral hydrogen atoms originating from the lunar surface, *Planet. Space Sci.*, *60*, 297–303.

Rosenblatt, P., and S. Charnoz (2012), On the formation of the Martian moons from a circum-Martian accretion disk, *Icarus*, *221*, 806–815.

Rutherford, J. A., and D. A. Vroom (1972), Formation of iron ions by charge transfer, *J. Chem. Phys.*, *57*(8), 3091–3093.

Sarantos, M., R. M. Killen, D. A. Glenar, M. Benna, and T. J. Stubbs (2012), Metallic species, oxygen and silicon in the lunar exosphere: Upper limits and prospects for LADEE measurements, *J. Geophys. Res.*, *117*, A03103, doi:10.1029/2011JA017044.

Schläppi, B., K. Altwegg, and P. Wurz (2008), Asteroid exosphere: A simulation for the ROSETTA flyby targets (2867) Steins and (21) Lutetia, *Icarus*, *195*, 674–685.

Shimazu, H. (2001), Three-dimensional hybrid simulation of solar wind interaction with unmagnetized planets, *J. Geophys. Res.*, *106*(A5), 8333–8342.

Sigmund, P. (1969), Theory of sputtering. I. Sputtering yield of amorphous and polycrystalline targets, *Phys. Rev.*, *184*, 383–416.

Smyth, W. H. (1992), Neutral cloud distribution in the Jovian system, *Adv. Space Res.*, *12*(8), 337–346.

Smyth, W. H., and M. R. Combi (1988), A general model for Io's neutral gas clouds. II. Application to the sodium cloud, *Astrophys. J.*, *328*, 888–918.

Smyth, W. H., and M. L. Marconi (1995), Theoretical overview and modeling of the sodium and potassium atmospheres of the Moon, *Astrophys. J.*, *443*, 371–392.

Soter, S. (1971), The dust belts of Mars, Rept. of Cent. for Radiophys. and Space Res. No. 462, Cornell Univ., Ithaca, New York.

Stebbings, R. F., A. C. H. Smith, and H. Ehrhardt (1964), Charge transfer between oxygen atoms and O^+ and H^+ ions, *J. Geophys. Res.*, *69*(18), 2349–2355.

Stern, S. A., K. D. Retherford, C. C. C. Tsang, P. D. Feldman, W. Pryor, and G. R. Gladstone (2012), Lunar atmospheric helium detections by the LAMP UV spectrograph on the Lunar Reconnaissance Orbiter, *Geophys. Res. Lett.*, *39*, L12202, doi:10.1029/2012GL051797.

Teolis, B. D., et al. (2010), Cassini finds an oxygen-carbon dioxide atmosphere at Saturn's icy moon Rhea, *Science*, *330*, 1813–1815.

Thompson, M. W., B. W. Farmery, and P. A. Newson (1968), A mechanical spectrometer for analyzing the energy distribution of sputtered atoms of copper and gold, *Philos. Mag.*, *18*(152), 361–383.

Tokar, R. L., R. E. Johnson, M. F. Thomsen, E. C. Sittler, A. J. Coates, R. J. Wilson, F. J. Crary, D. T. Young, and G. H. Jones (2012), Detection of exospheric O_2^+ at Saturn's moon Dione, *Geophys. Res. Lett.*, *39*, L03105, doi:10.1029/2011GL050452.

Valeille, A., M. R. Combi, S. W. Bougher, V. Tenishev, and A. F. Nagy (2009), Three-dimensional study of Mars upper thermosphere/ionosphere and hot oxygen corona: 2. Solar cycle, seasonal variations, and evolution over history, *J. Geophys. Res.*, *114*, E11006, doi:10.1029/2009JE003389.

Vernazza, P. et al. (2010), Meteorite analogs for Phobos and Deimos: Unraveling the origin of the Martian moons, *Meteorit. Planet. Sci. Suppl.*, *73*, 5076.

Veverka, J., and J. A. Burns (1980), The moons of Mars, *Annu. Rev. Earth Planet. Sci.*, *8*, 527–528.

Vignes, D., C. Mazelle, H. Rème, M. H. Acuña, J. E. P. Connerney, R. P. Lin, D. L. Mitchell, P. Cloutier, D. H. Crider, and N. F. Ness (2000), The solar wind interaction with Mars: Locations and shapes of the bow shock and the magnetic pile-up boundary from the observations of the MAG/ER experiment onboard Mars Global Surveyor, *Geophys. Res. Lett.*, *27*(1), 49–52.

Wieser, M., S. Barabash, Y. Futaana, M. Holmstrom, A. Bhardwaj, R. Sridharan, M. B. Dhanya, P. Wurz, A. Schaufelberger, and K. Asamura (2009), Extremely high reflection of solar wind protons as neutral hydrogen atoms from regolith in space, *Planet. Space Sci.*, *57*, 2132–2134.

Witasse, O., et al. (2014), Mars express investigations of Phobos and Deimos, *Planet. Space Sci.*, *102*, 18–34.

Wurz, P., U. Rohner, J. A. Whitby, C. Kolb, H. Lammer, P. Dobnikar, and J. A. Martín-Fernández (2007), The lunar exosphere: The sputtering contribution, *Icarus*, *191*, 486–496.

Yakshinskiy, B. V., and T. E. Madey (1999), Photon-stimulated desorption as a substantial source of sodium in the lunar atmosphere, *Nature*, *400*, 642–644.

Yakshinskiy, B. V., and T. E. Madey (2004), Photon-stimulated desorption of Na from a lunar sample: Temperature-dependent effects, *Icarus*, *168*, 53–59.